Inorganic Chemistry
Cite This: Inorg. Chem. 2019, 58, 14467−14477
Article
pubs.acs.org/IC

Rare-Earth Zirconate $Ln_2Zr_2O_7$ (Ln: La, Nd, Gd, and Dy) Powders, Xerogels, and Aerogels: Preparation, Structure, and Properties

Jorge Torres-Rodriguez,*[,†] Vanessa Gutierrez-Cano,[‡] Melita Menelaou,*[,†] Jaroslav Kaštyl,[†] Jaroslav Cihlář,[†] Serhii Tkachenko,[†] Jesús A. González,[‡] József Kalmár,[⊥,§] István Fábián,[⊥,§] István Lázár,[⊥,§] Ladislav Čelko,[†] and Jozef Kaiser[†]

[†]Central European Institute of Technology, Brno University of Technology, Purkyňova 123, Brno 61200, Czech Republic
[‡]Department of Earth Sciences and Condensed Matter Physics, University of Cantabria, Av. de los Castros, Santander 39005, Spain
[⊥]Department of Inorganic and Analytical Chemistry, University of Debrecen, Egyetem tér 1, Debrecen H-4032, Hungary
[§]MTA-DE Redox and Homogeneous Catalytic Reaction Mechanisms Research Group, Egyetem tér 1, Debrecen H-4032, Hungary

Supporting Information

ABSTRACT: The physicochemical properties of rare-earth zirconates can be tuned by the rational modification of their structures and phase compositions. In the present work, La^{3+}-, Nd^{3+}-, Gd^{3+}-, and Dy^{3+}-zirconate nanostructured materials were prepared by different synthetic protocols, leading to powders, xerogels, and, for the first time, monolithic aerogels. Powders were synthesized by the co-precipitation method, while xerogels and aerogels were synthesized by the sol−gel technique, followed by ambient and supercritical drying, respectively. Their microstructures, thermogravimetric profiles, textural properties, and crystallographic structures are reported. The co-precipitation method led to dense powders (S_{BET} < 1 $m^2\ g^{-1}$), while the sol−gel technique resulted in large surface area xerogels (S_{BET} = 144 $m^2\ g^{-1}$) and aerogels (S_{BET} = 168 $m^2\ g^{-1}$). In addition, the incorporation of lanthanide ions into the zirconia lattice altered the crystal structures of the powders, xerogels, and aerogels. Single-phase pyrochlores were obtained for $La_2Zr_2O_7$ and $Nd_2Zr_2O_7$ powders and xerogels, while defect fluorite structures formed in the case of $Gd_2Zr_2O_7$ and $Dy_2Zr_2O_7$. All aerogels contain a mixture of cubic and tetragonal ZrO_2 phases. Thus, a direct effect is shown between the drying conditions and the resulting crystalline phases of the nanostructured rare-earth zirconates.

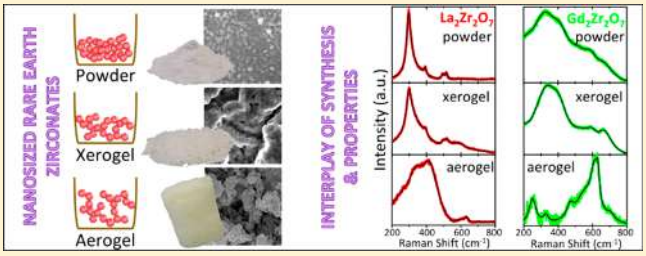

1. INTRODUCTION

Rare-earth zirconates with the chemical formula $Ln_2Zr_2O_7$ (where Ln is a trivalent rare-earth or lanthanide element) present a noticeable interest among scientific and industrial fields. The advantages that these materials demonstrate (i.e., low thermal conductivity, phase stability, and long luminescence lifetime after being doped with a suitable rare-earth ion such as Eu(III))[1−8] are related to their potential applications in electro/photocatalysis, magnetism, nuclear waste storage, and photoluminescent host materials.[9−14] In addition, the $Ln_2Zr_2O_7$ (LZ) materials are potential candidates for thermal-barrier coatings (TBCs).[15] Two crystal structures are characteristic for these materials: (i) the fluorite BO_6 (F) (space group $Fm\bar{3}m$, 4 formula units per unit cell) and (ii) the pyrochlore (P) $A_2B_2O_7$ (space group $Fd\bar{3}m$, 8 formula units per unit cell), which is a fluorite superstructure.[16] The pyrochlore lattice is a cation-ordered anion-deficient fluorite lattice, and for the completely ordered pyrochlore, the phase stability of the superstructure is primarily determined by the ionic radii of the A- and B-site cations. The pyrochlore lattice is favored if the value of the ionic radius ratio (RR = $r_{A^{3+}}/r_{B^{4+}}$) is between 1.46 and 1.80 at ambient conditions (e.g., $La_2Zr_2O_7$ RR = 1.61 and $Nd_2Zr_2O_7$ RR = 1.54).[17] In addition, pyrochlores show vacancies that make them good ionic conductors. Some of these materials can undergo an order−disorder phase transformation from pyrochlore to fluorite at temperatures beyond 1500 °C. This temperature transition strongly depends on the nature of the rare-earth ion along with the sample processing; for example, $Nd_2Zr_2O_7$, $Sm_2Zr_2O_7$, and $Gd_2Zr_2O_7$ undergo transitions between 1530 and 2300 °C.[17−21] The lanthanide zirconate $La_2Zr_2O_7$ undergoes a structural transformation under high-pressure conditions.[22,23] Typically, these materials can be prepared by a variety of synthetic methodologies (e.g., co-precipitation, sol−gel, molten salts, and combustion techniques; see Table S1 in the Supporting Information) that eventually lead to different chemical homogeneity, phase composition, and crystallite size.[24−26]

Presently, the high demands of modern living lead to a search for materials with superior properties. Aerogels are promising and advanced materials. Among other properties,

Received: July 4, 2019
Published: October 15, 2019

DOI: 10.1021/acs.inorgchem.9b01965
Inorg. Chem. 2019, 58, 14467−14477

aerogels in general have very low thermal conductivity (~0.01−0.02 W m^{-1} K^{-1}), high porosity (>90% v/v), and extremely low density (0.003−0.5 g cm^{-3}).[27−31] Solid, dry gels can conveniently be produced by the sol−gel technique, where once the wet gel has been formed, the subsequent drying process modifies the final material properties. Specifically, conventional evaporation of the solvent from the wet gel leads to a shrinkage of the structure yielding a xerogel. However, when the wet gel is subjected to a supercritical drying process, the porous structure of the gel is preserved and an aerogel forms.[32]

In the present work, we synthesized 4 rare-earth zirconates (i.e., $La_2Zr_2O_7$, $Nd_2Zr_2O_7$, $Dy_2Zr_2O_7$, and $Gd_2Zr_2O_7$) in the form of powders, xerogels, and aerogels. A comparative study was performed on the structural characteristics of these nanostructured materials by X-ray diffraction (XRD), Raman spectrometry, scanning electron microscopy (SEM), N_2 adsorption−desorption porosimetry, differential scanning calorimetry (DSC), and thermogravimetric analysis (TGA). By compiling all structural data, we show that, in addition to the chemical composition, the applied synthetic methods have a major impact on the final structural characteristics of the different nanostructured materials.

2. EXPERIMENTAL SECTION

2.1. Chemicals. Reagent-grade zirconium(IV) propoxide (70%) in 1-propanol, gadolinium nitrate hexahydrate (99.99%), and dysprosium nitrate hydrate (99.99%) were purchased from Sigma-Aldrich. Neodymium nitrate hexahydrate (99.99%), zirconium oxychloride oxide hydrate (99.99%), and 1-propanol anhydrous (99.9%) were purchased from Alfa Aesar. Nitric acid (65%) and acetone were obtained from Lach-ner. An aqueous ammonia solution (24%) was acquired from Penta, and lanthanum nitrate hexahydrate (96%) was purchased from Merck KGaA. Liquid CO_2 in a dip tube cylinder, used for the supercritical drying process, was purchased from SIAD (technical grade). All chemicals were used without further purification.

2.2. Synthesis of $Ln_2Zr_2O_7$ (LnZP) Powders. Rare-earth zirconate ($Ln_2Zr_2O_7$ or LZ) powders (where Ln^{3+} = La^{3+}, Nd^{3+}, Dy^{3+}, or Gd^{3+}) were prepared by the co-precipitation technique. In particular, $Ln(NO_3)_3{\cdot}xH_2O$ and zirconium(IV) oxychloride ($ZrOCl_2{\cdot}xH_2O$) were used as the precursor materials and were dissolved separately in deionized water. The ratio of the two reactants was 1:1, and the concentration of both solutions was 0.1 mol/L. Initially, 2 separate solutions were prepared and stirred for 30 min. Then, the solutions were mixed and stirred for 2 h. Aqueous ammonia (24%) was added dropwise to raise the pH to 11. The rate of dropping was about 30 drops min^{-1}. The pH value was monitored continuously with a digital pH meter (VWR pHenomenal 1100 L; glass pH electrode with a built-in 221 temperature sensor). As a result, gel-like precipitates formed in all 4 systems, which were subsequently filtered and washed twice with deionized water. Wet gels were dried at 120 °C for 12 h (Scheme 1). Calcination was carried out at 1000 °C in air for 5 h to obtain dry powders (hereafter, $La_2Zr_2O_7$ = LZP, $Nd_2Zr_2O_7$ = NZP, $Gd_2Zr_2O_7$ = GZP, and $Dy_2Zr_2O_7$ = DZP).

2.3. Synthesis of $Ln_2Zr_2O_7$ (LnZX) Xerogels. $Ln_2Zr_2O_7$ xerogels were prepared by the sol−gel technique. Initially, a solution containing 1-propanol (25 mL) (1-PrOH) and HNO_3 (0.45 mL) was prepared. Then $Ln(NO_3)_3{\cdot}xH_2O$ (1.47, 1.50, 1.53, and 1.49 g for La, Nd, Gd, and Dy, respectively) was added under mild stirring to form a transparent solution. Zirconium(IV) propoxide (1.53 mL) [$Zr(OPr)_4$] was slowly added in order to avoid any undesired precipitation. The Ln^{3+}:Zr^{4+} molar ratio was kept constant at 1:1. The as-prepared sol was poured into a beaker that was kept hermetically sealed until a rigid wet gel formed. The gels were not aged before drying. The beakers were unsealed. The wet gels were exposed to the dry laboratory air and left to dry spontaneously at room temperature for 48 h (Scheme 1). All samples were calcined at 1000 °C for 5 h (hereafter, $La_2Zr_2O_7$ = LZX, $Nd_2Zr_2O_7$ = NZX, $Gd_2Zr_2O_7$ = GZX, and $Dy_2Zr_2O_7$ = DZX).

Scheme 1. $Ln_2Zr_2O_7$ Nanostructured Materials Are Prepared Using a Variety of Drying Procedures[a]

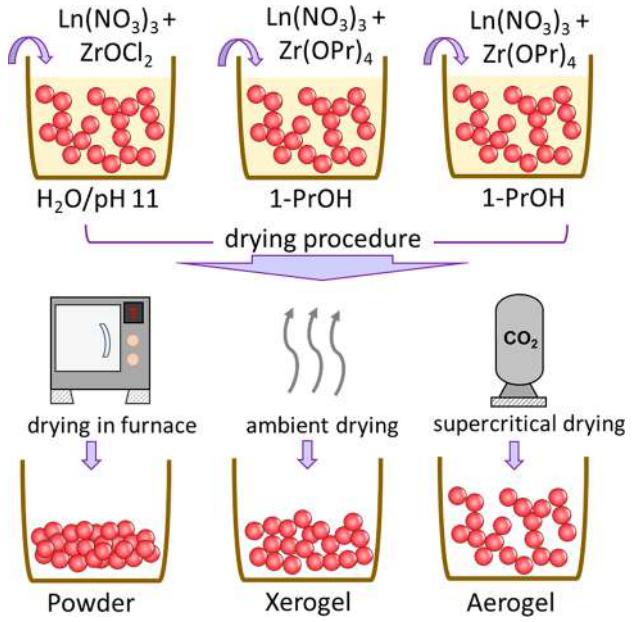

[a]Drying at 120 °C inside a furnace yields powders (LnZP), ambient evaporation of the solvent yields xerogels (LnZX), and supercritical drying yields aerogels (LnZA).

2.4. Synthesis of $Ln_2Zr_2O_7$ (LnZA) Aerogels. $Ln_2Zr_2O_7$ aerogels were prepared following a synthetic protocol similar to that used in the case of xerogels (section 2.3). However, to preserve the porous structure, all wet gels were transferred to perforated aluminum holders and aged for 24 h at room temperature in 1-propanol. During the aging step, the chemical reactions continue, and a reinforcement of the structure takes place. The stronger the gel network becomes, the better it can withstand the supercritical drying. Therefore, aged wet gels shrink and crack to a lesser degree than their non-aged xerogel counterparts, where the reactions are finished during the atmospheric drying conditions.

For aging, the wet gels were placed and soaked in a freshly prepared mixture of 1-propanol and acetone, and the mixture was changed every 24 h. For each cycle, the concentration of acetone was increased until pure acetone completely replaced the initial solvent (the steps are 1-propanol:acetone; 100:0, 75:25, 50:50, 25:75, 0:100). This solvent exchange process washed out any leftover of the reagents and the byproducts.

The last step was the supercritical drying of the gels using CO_2 (Scheme 1). The aged gels were placed into a high-pressure autoclave preliminarily filled with enough acetone to cover the samples. Subsequently, the autoclave was sealed and filled with liquid CO_2 at room temperature up to 56 bar. Then, the excess of acetone from the chamber was drained, so the liquid CO_2 could slowly diffuse through the open pores of the wet gel and replace the acetone that occupied the pores. By repeatedly exchanging the liquid CO_2 with fresh liquid CO_2, the complete elimination of acetone from the pore structure of the wet gels was achieved.[33] Afterward, the temperature was raised to 45 °C, incurring a pressure increment up to *ca.* 100 bar. These supercritical conditions were kept constant for 3 h for all samples. The autoclave was then depressurized at a rate of 2 bar min^{-1} and was finally cooled to room temperature. As a result, monolithic $Ln_2Zr_2O_7$ aerogels were obtained. All samples were calcined at 1000 °C for 5 h (hereafter, $La_2Zr_2O_7$ = LZA, $Nd_2Zr_2O_7$ = NZA, $Gd_2Zr_2O_7$ = GZA, and $Dy_2Zr_2O_7$ = DZA).

DOI: 10.1021/acs.inorgchem.9b01965
Inorg. Chem. 2019, 58, 14467−14477

2.5. Characterization of $Ln_2Zr_2O_7$ Nanostructured Materials. The microstructure of the powders, xerogels, and aerogels was studied using a high-resolution scanning electron microscope 460L Verios (FEI, Czech Republic). Samples for the scanning electron microscopy (SEM) studies were prepared on a carbon tape followed by the deposition of a conductive, thin carbon layer.

Thermogravimetric analysis (TGA), differential scanning calorimetry (DSC), and coupled mass spectrometry (MS) were carried out simultaneously (TGA-DSC-MS) in a Netzsch STA 409c/CD apparatus. Analyses were performed on the as-obtained materials in a synthetic air atmosphere (14 vol % O_2 in Ar) using Al_2O_3 crucibles with a heating rate of 10 °C min^{-1} from 20 to 1400 °C. The following MS signals of m/z were recorded: H_2O 18; CO 28; O_2 32; CO_2 44; and NO_x 14, 30, and 46.

Nitrogen gas adsorption−desorption measurements were performed on the as-obtained samples in an Autosorb iQ (Quantachrome Instruments, Boynton Beach, FL, USA) sorption analyzer at 77.4 K. The samples were degassed in vacuum at 180 °C for 12 h. ASiQwin version 4.0 (Quantachrome Instruments) was used for all calculations on the basis of the obtained isotherms. Specific surface area (S_{BET}) was calculated by using the Brunauer−Emmett−Teller (BET) method at 5 points in the linear range of the adsorption isotherms (P/P_0 = 0.10, 0.15, 0.20, 0.25, and 0.30) for all xerogel and aerogel samples. The micropore volume and the corresponding specific area were calculated using the t-plots (De Boer) method in addition to the adsorption isotherms. The pore size distribution of the samples was determined from the desorption isotherms using the Barrett−Joyner−Halenda (BJH) model (4 V/A).

X-ray diffraction (XRD) patterns from all samples were recorded using an X-ray diffractometer (Rigaku, Japan) operating in the Bragg−Brentano focusing geometry. A Cu Kα radiation source (λ = 1.5406 Å) was used as the X-ray source. The operating voltage and current of the instrument were kept at 40 kV and 30 mA, respectively. The XRD patterns were collected from 20° to 65° with a step size of 0.02° and a scanning speed of 0.1° min^{-1}.

Non-polarized Raman spectra were acquired in backscattering geometry with a Horiba T64000 Raman spectrometer equipped with a triple monochromator in the subtractive configuration (spectral resolution of 0.6 cm^{-1}) coupled to a confocal microscope. A 488 nm line of a Coherent Innova Spectrum 70C Ar^+−Kr^+ laser was used as the excitation source using a 20× objective with a laser power of 5 mW on each sample. A liquid-nitrogen-cooled CCD (Jobin-Yvon Symphony) was used as a detector.

3. RESULTS AND DISCUSSION

3.1. Surface Morphology by Scanning Electron Microscopy. SEM was performed on samples calcined at 1000 °C for 5 h (Figure 1). The microstructures of all powders (LnZP) show similar patterns with a coarse surface formed by grain sizes of *ca.* 100 nm (Figures 1a and S1). The primary particles are formed by randomly oriented grains (Figure S4a−d), which assemble to larger, dense microstructures with a high number of aggregates and a small number of micropores. The fundamental morphology of the powders is invariant to the lanthanide ion present in the structure (Figure S1a−b). In the case of the xerogels, the microstructure is composed of aggregates of spherical particles ($d \approx$ 100 nm). Despite evidence of a certain level of consolidation of these aggregates, a highly porous material was obtained in comparison with denser LnZP (Figures 1b and S2a−b). The surface morphology of the aerogels is composed of aggregated spherical nanoparticles ($d \approx$ 70 nm) with a large extent of open porosity distributed along the surface. Contrary to the LnZX samples, no evidence of particle consolidation is detected in the samples (Figures 1c and S3a−b).

The above-described differences in the morphologies are directly related to the applied synthetic methods used to produce powders, xerogels, and aerogels. For producing powders, the nanoparticles are precipitated in an aqueous medium. This and further calcination enhance particle growth effects that finally lead to dense, nonporous materials. On the contrary, the sol−gel method yields highly porous wet-gel networks. Eventually, the drying method of the wet gels and calcination determine the morphology and porosity of the final products. Drying of the wet gel under ambient conditions results in a certain degree of shrinkage accompanied by a loss of porosity, which is characteristic of xerogels. On the other hand, when the wet gel undergoes a supercritical drying process, a low-density and highly porous material (aerogel) is obtained.[18]

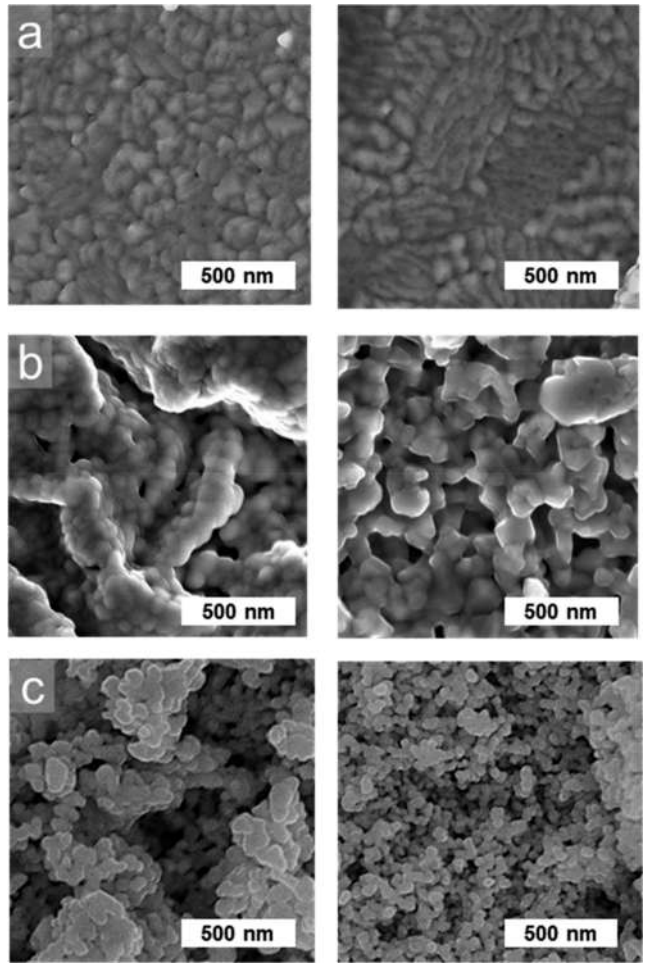

Figure 1. Scanning electron microscopy: surface morphology of the calcined $La_2Zr_2O_7$ and $Gd_2Zr_2O_7$ (a) powders, (b) xerogels, and (c) aerogels at 1000 °C/5 h. Additional SEM pictures are shown in the Supporting Information.

3.2. Thermal Analysis of the Nanostructured Materials. Thermal analysis of all the as-prepared LZ materials (LnZP, LnZX, and LnZA) was carried out in order to identify the presence of energetic processes taking place in the studied temperature range (25−1400 °C). First, for the LnZP samples, a broad endothermic peak can be observed from 50 to 200 °C, which is associated with the desorption of H_2O and accompanied by a weight loss of 8, 12, 5, and 6% for the LZP, NZP, GZP, and DZP samples, respectively (Figures S5a−d and S7). The desorption of H_2O continues up to ∼400 °C with the exception of the GZP, where it is observed at up to 600 °C (Figure S7c). In all samples, the combustion of residual

DOI: 10.1021/acs.inorgchem.9b01965
Inorg. Chem. 2019, 58, 14467−14477

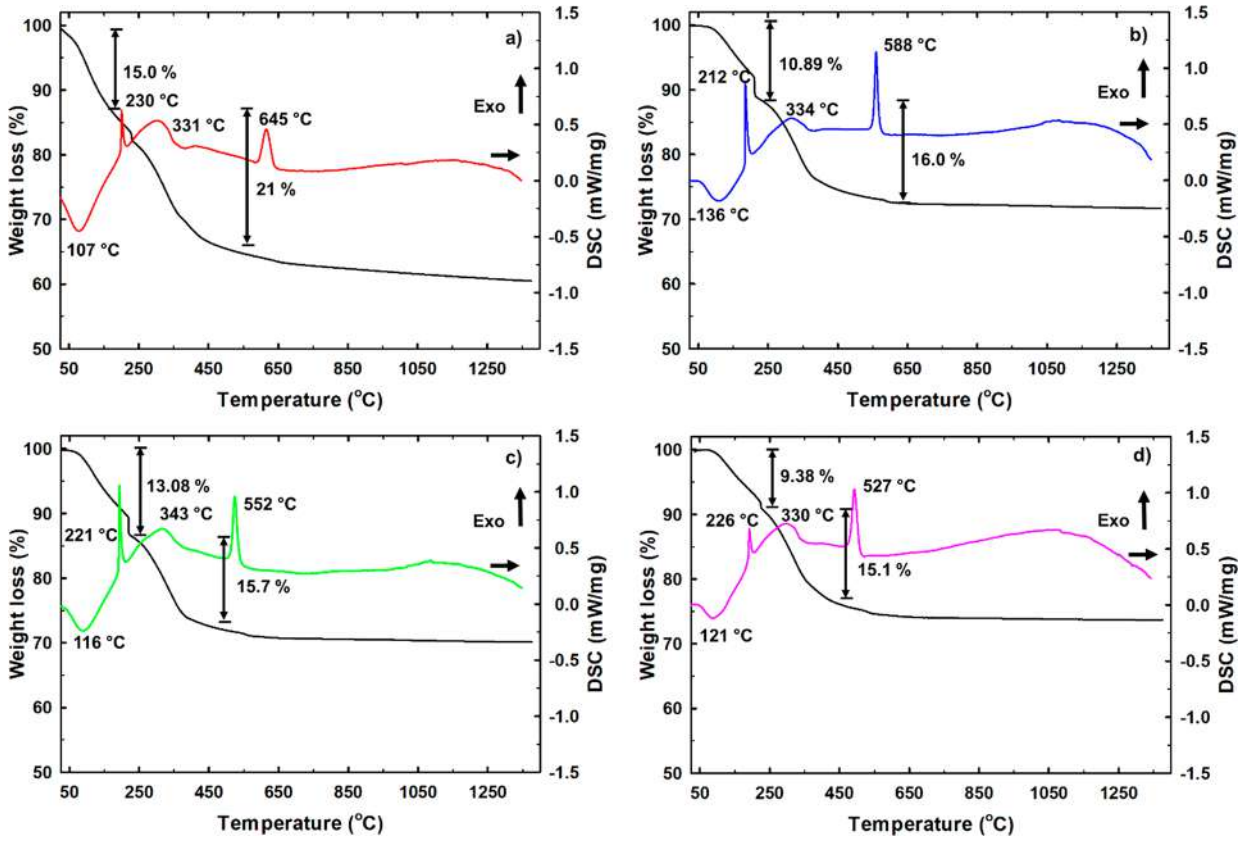

Figure 2. TGA/DSC patterns recorded from room temperature to 1400 °C of the as-obtained $Ln_2Zr_2O_7$ aerogels: (a) $La_2Zr_2O_7$, (b) $Nd_2Zr_2O_7$, (c) $Gd_2Zr_2O_7$, and (d) $Dy_2Zr_2O_7$.

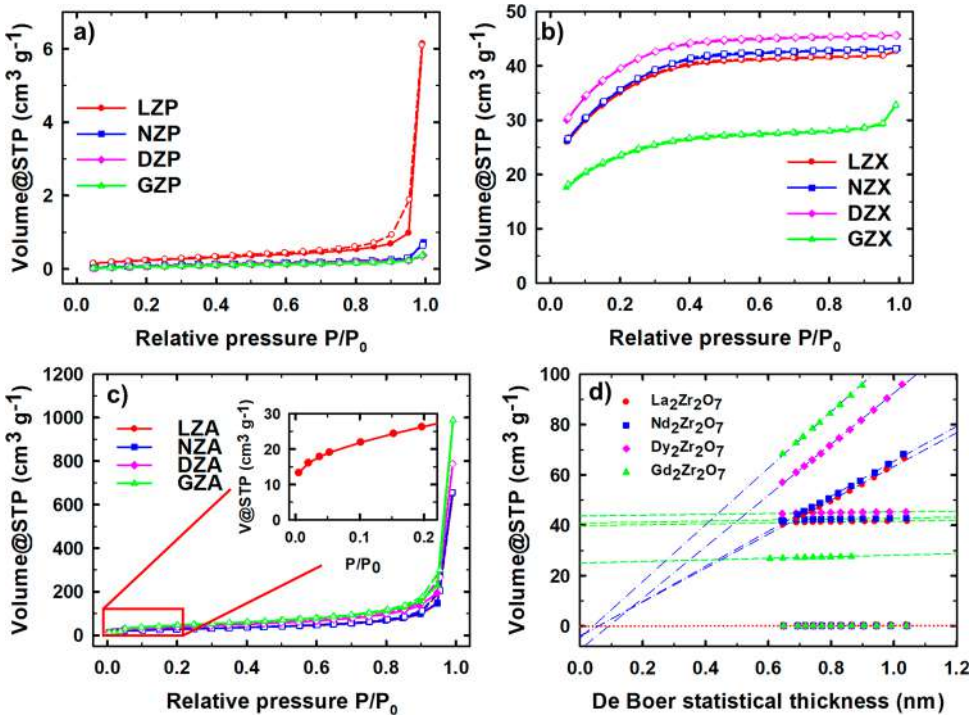

Figure 3. Nitrogen adsorption−desorption isotherms of (a) powders, (b) xerogels, and (c) aerogels. Inset: magnification of the $La_2Zr_2O_7$ aerogel adsorption isotherm at low relative pressures. (d) $V-t$ plot of all $Ln_2Zr_2O_7$ materials reported herein.

organic compounds took place in two stages leading to a weight loss of 4−8%. In the first stage, the removal of organic compounds is characterized by an exothermic peak between 200 and 400 °C. This effect is confirmed by the detection of CO, CO_2, and NO_x compounds in the MS data. Subsequently, the second process is associated with the exothermic curve

DOI: 10.1021/acs.inorgchem.9b01965
Inorg. Chem. 2019, 58, 14467−14477

Table 1. Summary of N_2 Sorption Analysis of Calcined Samples

			micropore		pore diameter		
sample	S_{BET} (m^2 g^{-1})	C value	area (m^2 g^{-1})	volume (cm^3 g^{-1})	average (nm)	characteristic[a](nm)	total pore volume (cm^3 g^{-1})
LZP	0.9	42 ± 4	0.2	0.000			0.010
NZP	0.3	12 ± 1	0.1	0.000			0.001
GZP	0.3	7 ± 1	0.1	0.000			0.001
DZP	0.4	5 ± 2	0.1	0.000			0.001
LZX	124 ± 18	162 ± 16	121	0.062	2.1	1.7	0.066
NZX	129 ± 19	111 ± 10	126	0.063	2.1	1.7	0.067
GZX	85 ± 12	129 ± 13	80	0.039	2.4	1.7	0.051
DZX	144 ± 19	128	142	0.068	2.0	1.7	0.071
LZA	100 ± 10	89 ± 8			40.0	120	1.0
NZA	102 ± 11	103 ± 9			39.9	110	1.02
GZA	168 ± 16	66 ± 6			36.5	131	1.53
DZA	139 ± 14	74 ± 6			35.2	119	1.22

[a]Characteristic pore diameter: estimated at the maximum of the distribution curve.

observed in the DSC plot between 600 and 800 °C. However, from the MS data, it can be seen that such a process ends beyond 1000 °C. Indeed, this continues in the NZP and DZP samples up to 1300 °C. The high-temperature appearance of organic compounds is related to the combustion of encapsulated synthesis residues.

The thermograms of the LnZX samples are shown in Figure S6a–d. The LZX sample shows an endothermic peak with a maximum at 123 °C. A small weight loss of 2.2% is present that is related to the desorption of water (MS plot, Figure S8a). All xerogels display a broad endothermic peak from 400 to 600 °C together with weight losses of 15.8, 8.8, 8.4, and 8.0% for the LZX, NZX, GZX, and DZX samples, respectively. These energetic processes are due to the degradation of nitrates and residual carbonate intermediate compounds from the synthesis procedure, as confirmed by the presence of CO, CO_2, and NO_x compounds in the MS plots. The highly adsorbed residual organics are released at *ca.* 700 °C for all samples. No additional energetic phenomenon was detected up to 1400 °C for any of the xerogels.

In the aerogel samples, the first endothermic peak is from 116 to 137 °C, accompanied by weight losses of 15.0, 10.9, 13.1, and 9.4% for the LZA, NZA, GZA, and DZA samples, respectively (Figure 2a–d). This peak is associated with the desorption of water according to the MS analysis (Figure S9). All of the LnZA samples showed a broad exothermic peak from *ca.* 150 to 400 °C with two maxima ranging between 221 and 234 °C and between 330 and 344 °C. According to the MS data (Figure S9), the first peak is mainly due to the rapid degradation of residual acetone and H_2O, while the second peak is the consequence of the thermal degradation of leftover compounds from the synthesis procedure (e.g., HNO_3, 1-propanol, etc.; Figure S9a–d). This exothermic process leads to mass losses of 21, 16, 15.7, and 15.1% for the LZA, DZA, GZA, and DZA samples, respectively. A sharp exothermic peak is present with a maxima at 645, 588, 552, and 527 °C for the LZA, NZA, GZA, and DZA samples, respectively. This event is observed in all the aerogel samples, and it is assigned to the amorphous-to-crystalline transition. No additional energetic phenomenon was detected up to 1400 °C. A summary of the analyzed thermal processes is presented in Table S2.

The decrease of the crystallization temperature of the aerogel samples correlates with the size of lanthanide ions in the periodic table from La^{3+} to Dy^{3+}. This effect can mainly be attributed to the nature of the lanthanide elements; the synthesis conditions have only secondary roles.[34−37]

3.3. Specific Surface Area and Pore Structure. In order to compare the textural properties of the calcined materials, N_2 adsorption−desorption isotherms were recorded and analyzed for all types of samples, as displayed in Figure 3. In addition, the pore size distributions of xerogels and aerogels were determined. However, in the case of powder samples, this analysis was not relevant because the apparent porosity is due to interparticle gaps rather than bulk porosity, as confirmed by the SEM images (section 3.1). The LnZP powders are characterized by type III isotherms, according to the IUPAC classification.[38] There is no inflection point on the isotherms, and therefore, there is no clearly distinguishable monolayer and multilayer formation of nitrogen (Figure 3a). The LnZX isotherms (Figure 3b) are of type I(b) with no hysteresis loop. Type I(b) isotherms are usually characteristic of materials having only micropores of d < 2.0 nm. The LnZA isotherms (Figure 3c) are of type II with a very small adsorbed nitrogen volume at low relative pressure (P/P_0) values and with practically no hysteresis loop (the magnified isotherm of LZA is shown in the inset of Figure 3c). In the V−t plot (Figure 3d), used for the determination of the microporosity of all the samples, the regression lines of powders, xerogels, and aerogels are displayed as red, green, and blue lines, respectively.

The adsorbed quantity of nitrogen on LnZX and LnZA is obviously larger than it is on LnZP samples. The adsorbed volume of gas on the LnZA and LnZX samples is roughly the same, but only at relative pressure values from 0 to 0.8. In the case of LnZA samples, the amount of adsorbed nitrogen steeply increases from P/P_0 = 0.8. The maximum adsorbed volume is almost 20 times higher than it is for LnZX samples and more than 150 times higher than it is for LnZP samples. This is due to the notable pore volume in LnZA samples (*cf.* Table 1). The specific surface areas (S_{BET}) are summarized in Table 1. The highest S_{BET} values are 144 m^2 g^{-1} for the Dy-xerogel sample (DZX) and 168 m^2 g^{-1} for the Gd-aerogel sample (GZA). The powders showed S_{BET} values below 1 m^2 g^{-1}. The S_{BET} values reported herein are significantly smaller than the previously reported values.[39−41] The definitive reason for the low S_{BET} values of powders is that the powders are aggregated into dense structures during the applied synthetic process (discussed in section 3.2). The measured apparent porosity is most probably due to the presence of interparticle

DOI: 10.1021/acs.inorgchem.9b01965
Inorg. Chem. 2019, 58, 14467−14477

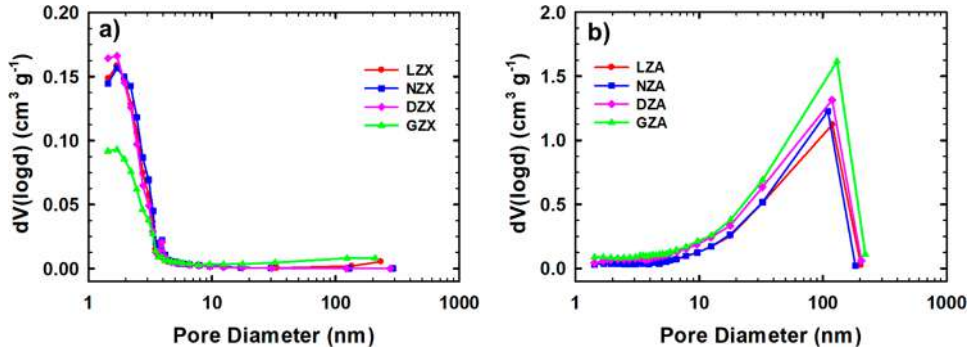

Figure 4. Pore size distributions of (a) xerogels and (b) aerogels are indicative of narrow microporosity and broad meso- and macro-porosity, respectively.

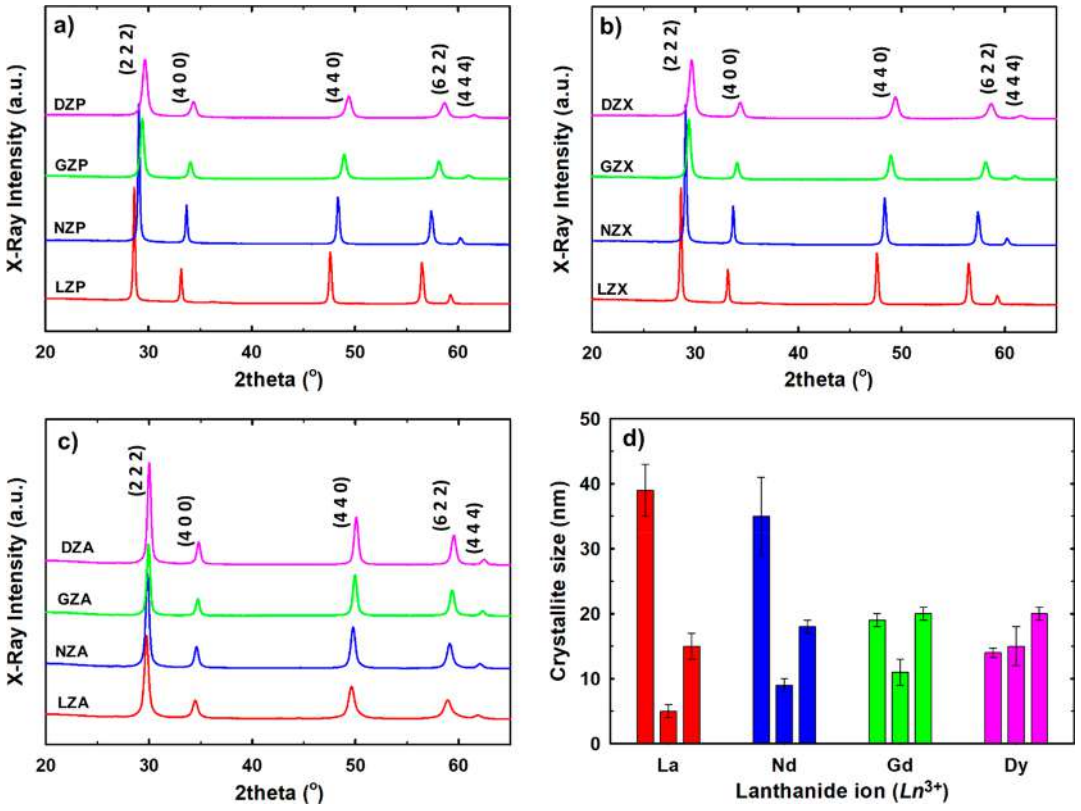

Figure 5. X-ray diffraction patterns of the calcined materials at 1000 °C: (a) powders (LnZP), (b) xerogels (LnZX), (c) aerogels (LnZA), and (d) calculated crystallite size as a function of the lanthanide ion (Ln^{3+}). For each element, from left to right, each bar corresponds to LnZP, LnZX, and LnZA, respectively.

gaps in the sample, but the bulk material of the powder is nonporous.

The *C* constant gives an indication of the force of the adsorbent−adsorbate interaction.[42] Although the aerogels represent the highest S_{BET} values (all aerogel samples have S_{BET} > 100 m^2 g^{-1}), the surfaces of xerogels seem to adsorb nitrogen with higher adsorption enthalpies because of the higher *C* constant values than those for aerogels. The reason for the apparently higher affinity of nitrogen toward the xerogels could be the existence of microporosity.[42,43] The *V*−*t* plots of all samples are shown in Figure 3d. The xerogels (green regression lines) have positive intercepts with the axis of adsorbed nitrogen volume that identifies the existence of microporosity, whereas the aerogels (blue regression lines) have practically zero intercepts, which is a sign of the absence of micropores. The powders (red regression lines) have positive intercepts; however, these intercepts are only slightly above zero. Thus, the S_{BET} of xerogels is strongly affected by a large micropore area (Table 1). The pore size distributions of xerogels and aerogels are shown in Figure 4a and Figure 4b, respectively.

The xerogels show very narrow pore size distributions, with pore sizes from 1 to 4 nm and an average pore size of *ca*. 2 nm. In contrast, the aerogels exhibit broad pore size distributions, with pore sizes ranging from 8 to 250 nm. The average pore sizes of aerogels are between 35 and 40 nm. In general, the total pore volume of LnZA is higher in comparison to its counterpart LnZX, indicating a higher sorption potential (see total pore volume in Table 1) with meso- and macro-porosity.

3.4. Phase Identification: Powder X-ray Diffraction and Crystallite Size. In order to investigate the crystalline phase of the calcined materials, X-ray powder diffraction

DOI: 10.1021/acs.inorgchem.9b01965
Inorg. Chem. 2019, 58, 14467−14477

(XRD) was carried out. The recorded patterns after calcination at 1000 °C are presented in Figure 5. Five main identifiable diffraction peaks were observed that correspond to the Miller indices (2 2 2), (4 0 0), (4 4 0), (6 2 2), and (4 4 4). These peaks can be assigned to both the fluorite (F) and pyrochlore (P) structures, whereas 2 extra diffraction peaks, namely (3 3 1) and (5 1 1), are unique to the pyrochlore structure (2θ at 36° and 45°, respectively). These two low-intensity peaks are sometimes difficult to detect, owing to the broadened nature of the XRD peaks of the nanostructured materials. Thus, fully understanding the results with respect to the synthetic protocol and/or the thermal treatment can be difficult.[16] Some examples from the literature include the isolation of single-phase pyrochlore $La_2Zr_2O_7$ powder by co-precipitation and subsequent calcination at 1000 °C[44] and of single-phase pyrochlore $La_2Zr_2O_7$ xerogel by the epoxide-assisted sol−gel technique and further heat treatment at 1000 °C.[45] Fuentes et al. obtained several $Gd_{2-x}Ln_xZr_2O_7$ materials with a fluorite structure by a mechanically induced reaction method from room temperature to 800 °C and further phase transition to the pyrochlore structure.[46] Thus, the pre/post processing has an important effect on the crystalline phase of the final product. This, coupled with the difficulty of detecting the P phase, makes the use of an additional technique, such as Raman spectrometry, necessary to determine the composition of the materials.

Peak broadening trends were observed in all materials, which can be indicative of different crystallite sizes due to the incorporation of the different lanthanide elements into the zirconia lattice. Thus, the crystallite size of all the materials was estimated by the Scherrer equation (Figure 5d).

As seen in Figure 5d, the LZP sample is composed of crystallites of 39 ± 4 nm, while the NZP, GZP, and DZP samples have crystallites of 35 ± 6, 19 ± 1, and 14 ± 0.7 nm, respectively. The size of the crystallites decreases with increasing atomic number of the incorporated lanthanide ion. Therefore, based on our findings, the incorporation of larger rare-earth element ions by the co-precipitation method more effectively inhibits the crystal growth.

On the other hand, the opposite effect was observed for xerogels and aerogels (Figure 5d). In this case, the higher the atomic number of the incorporated rare-earth element, the smaller the crystallites. For example, the LZX has a characteristic crystallite size of 5 ± 1 nm, while that of the DZX sample is 15 ± 3 nm. A similar phenomena occurred in the aerogel samples. Since all the materials were submitted to the same calcination process, the synthesis route we followed was crucial in determining the structure of each of the final products. The materials that were synthesized by the sol−gel method, namely xerogels and aerogels, have up to eight times smaller crystals than the powder samples synthesized by co-precipitation. In other words, the powder lanthanum sample has crystallite size of 39 ± 4 nm, whereas the xerogel and aerogel lanthanum sample have crystallite sizes of 5 ± 1 and 15 ± 2 nm, respectively.

3.5. Phase Identification by Raman Spectroscopy. In order to better understand the structures of the studied compounds and the effect of substituting the Ln^{3+} cation with different lanthanide ions, all calcined samples were analyzed by Raman spectroscopy at an ambient pressure. The differences between fluorite and pyrochlore XRD diffraction patterns are sometimes difficult to detect because of the low intensities of the superstructure (pyrochlore) peaks.[47] Raman spectroscopy is a useful tool to provide information about the oxygen cation vibrations and distinguish between the phases and the mixture of the phases.

Figure 6 shows the Raman spectra of the powder samples at ambient conditions. $Ln_2Zr_2O_7$ compounds with a pyrochlore

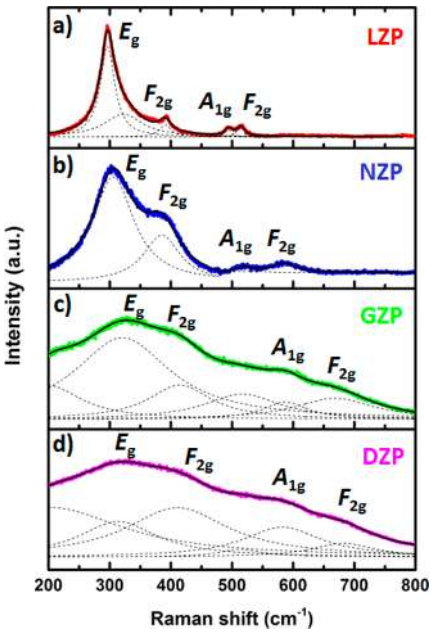

Figure 6. Raman spectra of LnZP materials at ambient conditions: (a) LZP, (b) NZP, (c) GZP, and (d) DZP. The vibrational modes of the pyrochlores and/or fluorite structures are identified.

structure belong to the $Fd\bar{3}m$ space group and have six Raman active modes in the center of the Brillouin zone, which according to group theory are[47,48]

$$\Gamma = A_{1g} + E_g + 4F_{2g}$$

However, in the Raman spectra of the pyrochlore-type LZP sample, only four bands are observed (Figure 6a). This is probably due to the use of a nonpolarized Raman method. In order to observe the remaining F_{2g} modes, another polarization method should be used. The observed Raman bands of LZP can be assigned as follows: the band at 514 cm^{-1} corresponds to the A_{1g} mode, and it is related to the O−Zr−O bending vibrations of the ZrO_6 octahedron; the most intense band at 297 cm^{-1} is assigned to the E_g mode, and it is related to the Zr−O bending vibrations; and the bands at 391 and 495 cm^{-1} are assigned to the La−O and Zr−O stretching vibrations, respectively, with the contribution of bending vibrations of the F_{2g} modes.[49−51] Raman band analysis complements XRD results and clearly shows the ordered pyrochlore structure of LZP. Similar characteristics can be observed in the Raman spectra of NZP (Figure 6b). The A_{1g} mode related to the O−Zr−O bending vibrations appears at 519 cm^{-1}. The E_g mode shows higher intensity, and it is observed at 306 cm^{-1}. Finally, the bands located at 385 and 585 cm^{-1} correspond to F_{2g} vibration modes.[49,52] Interestingly, the main peak of both pyrochlore-like compounds, located at *ca.* 300 cm^{-1}, is broader when La^{3+} is replaced by Nd^{3+}, leading to a decrease of local order.

Moreover, the Raman spectrum of a fluorite structure is characterized by a single Raman active mode (F_{2g} at *ca.* 466 cm^{-1}), which is very broad and reflects the disorder introduced

DOI: 10.1021/acs.inorgchem.9b01965
Inorg. Chem. 2019, 58, 14467−14477

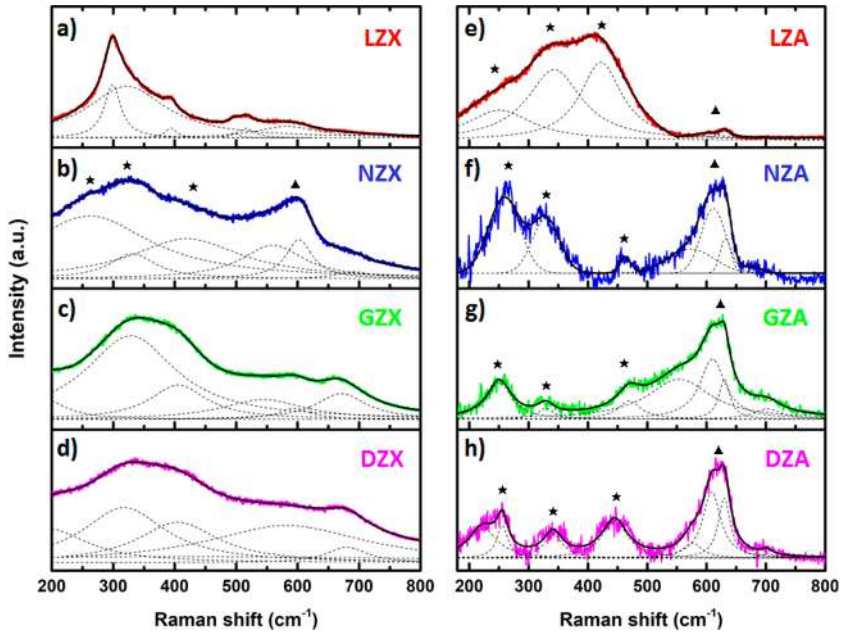

Figure 7. Raman spectra of LnZX and LnZA materials at ambient conditions: (a) LZX, (b) NZX, (c) GZX, (d) DZX, (e) LZA, (f) NZA, (g) GZA, and (h) DZA. Vibrational modes of tetragonal zirconia are depicted with stars (*), and vibrational modes of the LnZ cubic phase are depicted with triangles (▲).

by the random distribution of oxygen atoms in the anion sites. In the case of DZP and GZP samples, Raman spectra do not show the single band of a typical fluorite structure, but several bands can be observed (Figures 6c–d). However, both spectra are very broad, and the contributions of the different vibrational modes are not easy to distinguish without fitting Lorentzian functions. In spite of the Raman spectra showing peaks of pyrochlore structures, XRD measurements (Figure 5) do not distinguish whether the DZP and GZP samples have pyrochlore or defect fluorite structures. Taking this into consideration, previous publications suggest that DZP and GZP compounds represent disordered fluorite structures with some order at the microdomain levels.[50] This effect was observed in compounds synthesized by the sol–gel and solvothermal synthesis routes as well as by co-precipitation and solid state reactions.[49,50,53]

The combination of XRD and Raman spectroscopy shows the change of structure in LnZP materials when replacing the Ln site by either La^{3+}, Nd^{3+}, Gd^{3+}, or Dy^{3+} cations, leading to a transformation from an ordered pyrochlore structure to a disordered fluorite structure with a certain order at the microdomains. The tendency to have a disordered structure increases when moving from La^{3+} to Dy^{3+} in the lanthanide series.

Similar behavior is observed in the xerogel samples (Figure 7a–d). The Raman spectrum of LZX suggests a pyrochlore structure, where the E_g mode appears at 298 cm^{-1}, the A_{1g} mode appears at 517 cm^{-1}, and the F_{2g} modes appear at 392 and 497 cm^{-1} (Figure 7a). Compared to the powder LZP sample, the LZX spectrum is slightly broadened. The Raman spectra of DZX and GZX are also very similar to the spectra of the powder samples. Disordered fluorite structures with remnant contributions of pyrochlore are observed (Figures 7c–d). In the case of the NZX, significant spectral differences can be found when compared to the Raman spectrum of the powder. As explained below, the spectrum of NZX (Figure 7b) is very broad, and the fitting unveils vibrational contributions that are similar to those of the NZA.

Finally, the Raman spectra of the aerogels are shown in Figure 7e–h. As previously mentioned, a fluorite-related structure should consist of a single F_{2g} mode located between 400 and 500 cm^{-1}. However, the Raman spectrum of cubic LnZA at ambient conditions is characterized by a broad peak near 530–670 cm^{-1} in addition to poorly defined bands associated with the disordered oxygen sublattice.[54] This trend is clearly observed in three of our synthesized aerogels (i.e., in the NZA, DZA, and GZA samples), where a cubic structure is predominant (Figures 7f–h). This structure is defined by a broad band found between 500 and 650 cm^{-1}, having its maximum between 606 and 630 cm^{-1}. It was not possible to identify whether this structure is fluorite or pyrochlore. Additional broad bands are also observed at 250–259, 328–339, and 450–470 cm^{-1}. These bands may be attributed to trace amounts of tetragonal ZrO_2, which is characterized by the vibrational modes located at 266, 326, 474, 616, and 646 cm^{-1}.[55] This contrasts cubic ZrO_2, which is known to display a single Raman band.[56] We did not observe this feature by X-ray diffraction due to the peak broadening and the similar peak positions of ZrO_2 diffraction patterns.[54] Similar characteristics were previously observed by Chervin et al. in yttria-stabilized zirconia (YSZ) aerogels. In the case of the LZA spectrum, all the above mentioned peaks are also present but with a change of relative intensities. A broad band between 200 and 500 cm^{-1} contains the tetragonal-related bands. A possible explanation for the observation of ZrO_2 tetragonal modes by Raman spectroscopy and not by XRD could be the small amount of this phase, which is below the detection limits of XRD (~3 wt % in a two-phase mixture).

As mentioned earlier, xerogels and aerogels were prepared under the same conditions to form the wet gels, while the drying method was crucial in determining the final structures and properties of the materials. LZX and NZX samples contain single-phase pyrochlore, while in the case of GZX and DZX

DOI: 10.1021/acs.inorgchem.9b01965
Inorg. Chem. 2019, 58, 14467–14477

xerogels, a fluorite structure is dominant along with some amount of pyrochlore. On the other hand, LZA, NZA, GZA, and DZA are a mixture of cubic $Ln_2Zr_2O_7$ and tetragonal ZrO_2 crystalline phases. In addition, as stated in section 3.1, the supercritical drying process had a major effect on the crystallite size of the aerogels.

These results suggest that the applied supercritical drying conditions set the crystal structure, which in turn determines macroscopic physicochemical properties. The influence of supercritical drying on material properties has already been reported in other types of oxide materials.[57] For example, TiO_2 with a 100% anatase phase was obtained directly from a low-temperature supercritical drying process in a mixture of CO_2 and isopropanol.[58] Also, TiO_2 aerogel systems with a single-phase anatase and high crystallinity were obtained by supercritical drying in CO_2, while the ambient pressure drying process resulted in a mixture of anatase and rutile phases.[59] In another study, TiO_2 aerogels demonstrated better photocatalytic degradation due to the higher crystallinity grade than their xerogel counterparts.[60]

4. CONCLUSIONS

Rare-earth zirconate $Ln_2Zr_2O_7$ (Ln = La, Nd, Gd, and Dy) powders, xerogels, and aerogels were successfully prepared. Powders were synthesized via co-precipitation, while wet gels were prepared via the sol–gel technique. Modifying the drying protocol of the wet gels led to xerogels (LnZX), by ambient drying, and to aerogels (LnZA), by drying in supercritical CO_2. All materials were calcined at 1000 °C. The synthesized powders consist of nanoparticles arranged in a dense microstructure with a very small specific surface area (S_{BET} < 1 $m^2\ g^{-1}$) and porosity. The xerogels and the aerogels are built from nanometer-sized globules. Their specific surface areas are high and reach 168 $m^2\ g^{-1}$ for the $Gd_2Zr_2O_7$. The xerogels are microporous, and the aerogels display a large size distribution of pores.

The crystallinity of the materials was investigated by a combination of XRD and Raman spectroscopy. The $La_2Zr_2O_7$ and $Nd_2Zr_2O_7$ powders and xerogels display a single-phase-ordered pyrochlore structure, while the $Gd_2Zr_2O_7$ and $Nd_2Zr_2O_7$ powders and xerogels are in a fluorite crystalline phase. All $Ln_2Zr_2O_7$ aerogels contain a mixture of cubic and tetragonal ZrO_2 phases. The co-precipitation method used for the production of powders promotes crystallite size growth, which contrasts with the sol–gel process used for producing aerogels and xerogels. Larger crystallites are present in the aerogels than in their xerogel counterparts. All the structural investigations unanimously proved that the synthetic procedure applied to prepare the given material and the drying conditions have a direct and significant effect on the crystalline phase and the crystallite size of rare-earth zirconates of $Ln_2Zr_2O_7$ composition.

■ ASSOCIATED CONTENT

Supporting Information

The Supporting Information is available free of charge on the ACS Publications website at DOI: 10.1021/acs.inorgchem.9b01965.

Additional results from thermogravimetric analysis and scanning electron microscopy (PDF)

■ AUTHOR INFORMATION

Corresponding Authors

*E-mail: JorgeAlberto.TorresRodriguez@ceitec.vutbr.cz.
*E-mail: Melita.Menelaou@ceitec.vutbr.cz.

ORCID

Jorge Torres-Rodriguez: 0000-0002-2210-472X
Vanessa Gutierrez-Cano: 0000-0002-6751-8870
József Kalmár: 0000-0002-2422-6106
István Fábián: 0000-0002-4467-2912

Notes

The authors declare no competing financial interest.

■ ACKNOWLEDGMENTS

This research has been financially supported by the Ministry of Education, Youth, and Sports of the Czech Republic under the Project CEITEC 2020 (LQ1601). This work was supported by the ESF under Project CZ.02.2.69/0.0/0.0/18_070/0009469. Part of this work was carried out with the support of the CEITEC Nano Research Infrastructure (MEYS CR, 2016–2019). This work was supported by the National Research, Development, and Innovation Office; the Hungarian Science Foundation (OTKA: FK_17-124571); and by GINOP-2.3.2-15-2016-00041 project. This project is co-financed by the European Union and the European Regional Development Fund. This work was supported by CA18125 - Advanced Engineering and Research of AeroGels for Environment and Life Sciences.

■ REFERENCES

(1) Gupta, S. K.; Ghosh, P. S.; Reghukumar, C.; Pathak, N.; Kadam, R. M. Experimental and theoretical approach to account for green luminescence from $Gd_2Zr_2O_7$ pyrochlore: exploring the site occupancy and origin of host-dopant energy transfer in $Gd_2Zr_2O_7$:Eu^{3+}. *RSC Adv.* **2016**, *6*, 44908.

(2) Zhang, J. M.; Lian, J.; Fuentes, A. F.; Zhang, F. X.; Lang, M.; Lu, F. Y.; Ewing, R. C. Enhanced radiation resistance of nanocrystalline pyrochlore $Gd_2(Ti_{0.65}Zr_{0.35})_2O_7Gd_2(Ti_{0.65}Zr_{0.35})_2O_7$. *Appl. Phys. Lett.* **2009**, *94*, 243110.

(3) Dey, S.; Drazin, J. W.; Wang, Y. Q.; Valdez, J. A.; Holesinger, T. G.; Uberuaga, B. P.; Castro, R. H. R. Radiation Tolerance of Nanocrystalline Ceramics: Insights from Yttria Stabilized Zirconia. *Sci. Rep.* **2015**, *5*, 7746.

(4) Soyez, G.; Eastman, J. A.; Thompson, L. J.; Bai, G. R.; Baldo, P. M.; McCormick, A. W.; DiMelfi, R. J.; Elmustafa, A. A.; Tambwe, M. F.; Stone, D. S. Grain-size-dependent thermal conductivity of nanocrystallineyttria-stabilized zirconia films grown by metal-organic chemical vapor deposition. *Appl. Phys. Lett.* **2000**, *77*, 1155.

(5) Zhang, Y. W.; Jin, S.; Yang, Y.; Li, G. B.; Tian, S. J.; Jia, J. T.; Liao, C. S.; Yan, C. H. Electrical conductivity enhancement in nanocrystalline $(RE_2O_3)_{0.08}(ZrO_2)_{0.92}$ (RE = Sc, Y)-$(RE_2O_3)_{0.08}(ZrO_2)_{0.92}$ (RE = Sc, Y) thin films. *Appl. Phys. Lett.* **2000**, *77*, 3409.

(6) Gupta, S. K.; Zuniga, J. P.; Ghosh, P. S.; Abdou, M.; Mao, Y. Correlating Structure and Luminescence properties of undoped and Eu^{3+}-doped $La_2Hf_2O_7$ nanoparticles prepared with different coprecipitating pH values through experimental and theoretical studies. *Inorg. Chem.* **2018**, *57*, 11815.

(7) Eagleman, Y.; Weber, M.; Chaudhry, A.; Derenzo, S. Luminescence study of cerium-doped $La_2Hf_2O_7$: Effects due to trivalent and tetravalent cerium and oxygen vacancies. *J. Lumin.* **2012**, *132*, 2889.

(8) Gupta, S. K.; Ghosh, P. S.; Reghukumar, C.; Pathak, N.; Kadam, R. M. Experimental and theoretical approach to account for green luminescence from $Gd_2Zr_2O_7$ pyrochlore: exploring the site

DOI: 10.1021/acs.inorgchem.9b01965
Inorg. Chem. 2019, 58, 14467–14477

occupancy and origin of host-dopant energy transfer in $Gd_2Zr_2O_7$:Eu^{3+}. *RSC Adv.* **2016**, *6*, 44908.
(9) Lumpkin, G. R. Alpha-Decay Damage and Aqueous Durability of Actinide Host Phases in Natural Systems. *J. Nucl. Mater.* **2001**, *289*, 136.
(10) Perriot, R.; Dholabhai, P. P.; Uberuaga, B. P. The role of surfaces, chemical interfaces, and disorder on plutonium incorporation in pyrochlores. *Phys. Chem. Chem. Phys.* **2016**, *18*, 22852.
(11) Park, J.; Risch, M.; Nam, G.; Park, M.; Shin, T. J.; Park, S.; Kim, M. G.; Shao-Horn, Y.; Cho, J. Single crystalline pyrochlore nanoparticles with metallic conduction as efficient bi-functional oxygen electrocatalysts for Zn-air batteries. *Energy Environ. Sci.* **2017**, *10*, 129.
(12) Oh, S. H.; Black, R.; Pomerantseva, E.; Lee, J.; Nazar, L. F. Synthesis of a metallic mesoporous pyrochlore as a catalyst for lithium-O_2 batteries. *Nat. Chem.* **2012**, *4*, 1004.
(13) Feng, T.; Clarke, D. R.; Jiang, D.; Xia, J.; Shi, J. Neodymium zirconate($Nd_2Zr_2O_7$) transparent ceramics as a solid state laser material. *Appl. Phys. Lett.* **2011**, *98*, 151105.
(14) Boaro, M.; Pappacena, A.; Abate, C.; Ferluga, M.; Llorca, J.; Trovarelli, A. Effect of redox treatments on $Ce_{0.50}Zr_{0.50}O_2$ based solid oxide fuel cell anodes Power Sources. *J. Power Sources* **2014**, *270*, 79.
(15) Vassen, R.; Cao, X.; Tietz, F.; Basu, D.; Stöver, D. Zirconates as New Materials for Thermal Barrier Coatings. *J. Am. Ceram. Soc.* **2000**, *83*, 2023.
(16) Aleshin, E.; Roy, R. Crystal Chemistry of Pyrochlore. *J. Am. Ceram. Soc.* **1962**, *45*, 18.
(17) Subramanian, M.A.; Aravamudan, G.; Subba Rao, G.V. Oxide pyrochlores — A review. *Prog. Solid State Chem.* **1983**, *15*, 55.
(18) Michel, D.; Perez y Jorba, M.; Collongues, R. Etude de la transformationordre-desordre de la structurefluorite a la structure pyrochlore pour des phases (1-x) ZrO_2 x Ln_2O_3. *Mater. Res. Bull.* **1974**, *9*, 1457.
(19) Michel, D.; Perez, M.; Collongues, J. R. Study by Raman spectroscopy of order-disorder phenomena occurring in some binary oxides with fluorite-related structures. *J. Raman Spectrosc.* **1976**, *5*, 163.
(20) Rushton, M. J. D.; Grimes, R. W.; Stanek, C. R.; Owens, S. Predicted pyrochlore to fluorite disorder temperature for $A_2Zr_2O_7$ compositions. *J. Mater. Res.* **2004**, *19*, 1603.
(21) Zuniga, J. P.; Gupta, S. K.; Abdou, M.; De Santiago, H. A.; Puretzky, A. A.; Thomas, M. P.; Guiton, B. S.; Liu, J.; Mao, Y. Size, structure, and luminescence of $Nd_2Zr_2O_7$ nanoparticles by molten salt synthesis. *J. Mater. Sci.* **2019**, *54*, 12411.
(22) Niu, J.; Wu, X.; Zhang, H.; Qin, S. Pressure-induced phase transition of $La_2Zr_2O_7$ and $La_{0.5}Gd_{1.5}O_7$ pyrochlore. *RSC Adv.* **2019**, *9*, 18954.
(23) Xiao, H. Y.; Zhang, F. X.; Gao, F.; Lang, M.; Ewing, R. C.; Weber, W. J. Zirconatepyrochlores under high pressure. *Phys. Chem. Chem. Phys.* **2010**, *12*, 12472.
(24) Mandal, B. P.; Banerji, A.; Sathe, V.; Deb, S. K.; Tyagi, A. K. Order-Disorder Transition in Nd_2-y$Gd_yZr_2O_7$ Pyrochlore Solid Solution: An X-Ray Diffraction and Raman Spectroscopic Study. *J. Solid State Chem.* **2007**, *180*, 2643.
(25) Tang, Z.; Huang, Z.; Qi, J.; Guo, X.; Han, W.; Zhou, M.; Peng, S.; Lu, T. Synthesis and characterization of $Gd_2Zr_2O_7$ defect-fluorite oxide nanoparticles via a homogeneous precipitation-solvothermal method. *RSC Adv.* **2017**, *7*, 54980.
(26) Zhang, Y. W.; Xu, G.; Yan, Z. G.; Yang, Y.; Liao, C. S.; Yan, C. H. Nanocrystalline rare earth stabilized zirconia: solvothermal synthesis via heterogeneous nucleation-growth mechanism, and electrical properties. *J. Mater. Chem.* **2002**, *12*, 970.
(27) Koebel, M.; Rigacci, A.; Achard, P. Aerogel-based thermal superinsulation: an overview. *J. Sol-Gel Sci. Technol.* **2012**, *63*, 315.
(28) Chaudhary, J. P.; Vadodariya, N.; Nataraj, S. K.; Meena, R. Chitosan-Based Aerogel Membrane for Robust Oil-in-Water Emulsion Separation. *ACS Appl. Mater. Interfaces* **2015**, *7*, 24957.
(29) Guilminot, E.; Fischer, F.; Chatenet, M.; Rigacci, A.; Berthon-Fabry, S.; Achard, P.; Chainet, E. Use of cellulose-based carbon aerogels as catalyst support for PEM fuel cell electrodes: Electrochemical characterization. *J. Power Sources* **2007**, *166*, 104.
(30) Bechthold, M.; Weaver, J. C. Materials science and architecture. *Nat. Rev. Mat* **2017**, *2*, 1.
(31) Ziegler, C.; Wolf, A.; Liu, W.; Herrmann, A.-K.; Gaponik, N.; Eychmüller, A. Modern Inorganic Aerogels. *Angew. Chem., Int. Ed.* **2017**, *56*, 13200.
(32) Rechberger, F.; Niederberger, M. Synthesis of aerogels: from molecular routes to 3-dimensional nanoparticle assembly. *Nanoscale Horiz* **2017**, *2*, 6.
(33) Lázár, I.; Fábián, I. A Continuous Extraction and Pumpless Supercritical CO2 Drying System for Laboratory-Scale Aerogel Production. *Gels* **2016**, *2*, 26.
(34) Ozawa, M.; Kimura, M. Preparation and characterization of zirconium dioxide catalyst supports modified with rare earth elements. *J. Less-Common Met.* **1991**, *171*, 195.
(35) Gorban, O.; Synyakina, S.; Volkova, G.; Gorban, S.; Konstantiova, T.; Lyubchik, S. Formation of metastable tetragonal zirconia nanoparticles: Competitive influence of the dopants and surface state. *J. Solid State Chem.* **2015**, *232*, 249.
(36) Torres-Rodriguez, J.; Kalmár, J.; Menelaou, M.; Čelko, L.; Dvořak, K.; Cihlář, J.; Cihlař, J.; Kaiser, J.; Győri, E.; Veres, P.; Fábián, I.; Lázár, I. Heat treatment induced phase transformations in zirconia and yttria-stabilized zirconia monolithic aerogels. *J. Supercrit. Fluids* **2019**, *149*, 54.
(37) Shukla, S.; Seal, S. Mechanisms of room temperature metastable tetragonal phase stabilisation in zirconia. *Int. Mater. Rev.* **2005**, *50*, 45.
(38) Thommes, M.; Kaneko, K.; Neimark, A. V.; Olivier, J. P.; Rodriguez-Reinoso, F. Physisorption of gases, with special reference to the evaluation of surface area and pore size distribution (IUPAC Technical Report). *Pure Appl. Chem.* **2015**, *87*, 1 DOI: 10.1515/pac-2014-1117.
(39) Kong, L.; Karatchevtseva, I.; Gregg, D. J.; Blackford, M. G.; Holmes, R.; Triani, G. A Novel Chemical Route to Prepare $La_2Zr_2O_7$ Pyrochlore. *J. Am. Ceram. Soc.* **2013**, *96*, 935.
(40) Joulia, A.; Renard, E.; Tchou-Kien, D.; Vardelle, M.; Rossignol, S. Rare Earth Oxides Pyrochlore Compounds by Soft Chemistry. *Advanced Ceramic Coatings and Materials for Extreme Environments II*; Zhu, D., Lin, H., Zhou, Y., Hwang, T., Halbig, M., Mathur, S., Eds.; The American Ceramic Society. 2012. DOI: 10.1002/9781118217474.ch5.
(41) Wang, S.; Li, W.; Wang, S.; Jiang, J.; Chen, Z. Synthesis of well-defined hierarchical porous $La_2Zr_2O_7$ monoliths via non-alkoxide sol-gel process accompanied by phase separation. *Microporous Mesoporous Mater.* **2016**, *221*, 32.
(42) International Organization for Standardization. Determination of the specific surface area of solids by gas adsorption - BET method. ISO 9277:2010(E). **2010**.
(43) Thommes, M. Physical Adsorption Characterization of Nanoporous Materials. *Chem. Ing. Tech.* **2010**, *82*, 1059.
(44) Chen, H.; Gao, Y.; Liu, Y.; Luo, H. Coprecipitation synthesis and thermal conductivity of $La_2Zr_2O_7$. *J. Alloys Compd.* **2009**, *480*, 843.
(45) Wang, S.; Li, W.; Wang, S.; Chen, Z. Synthesis of mesoporous $La_2Zr_2O_7$ with high surface area by combining epoxide-mediated sol-gel process and solvothermal treatment. *Microporous Mesoporous Mater.* **2016**, *234*, 137.
(46) Fuentes, A. F.; Montemayor, S. M.; Maczka, M.; Lang, M.; Ewing, R. C.; Amador, U. A Critical Review of Existing Criteria for the Prediction of Pyrochlore Formation and Stability. *Inorg. Chem.* **2018**, *57*, 12093.
(47) Zhou, L.; Huang, Z.; Qi, J.; Feng, Z.; Wu, D.; Zhang, W.; Yu, X.; Guan, Y.; Chen, X.; Xie, L.; Sun, K.; Lu, T. Thermal-Driven Fluorite-Pyrochlore-Fluorite Phase Transitions of GdZrO Ceramics Probed in Large Range of Sintering Temperature. *Metall. Mater. Trans. A* **2016**, *47*, 623.
(48) Shimamura, K.; Arima, T.; Idemitsu, K.; Inagaki, Y. Thermophysical Properties of Rare-Earth-Stabilized Zirconia and

DOI: 10.1021/acs.inorgchem.9b01965
Inorg. Chem. 2019, 58, 14467−14477

Zirconate Pyrochlores as Surrogates for Actinide-Doped Zirconia. *Int. J. Thermophys.* **2007**, *28*, 1074.
(49) Wang, S.; Li, W.; Wang, S.; Chen, Z. Synthesis of nanostructured $La_2Zr_2O_7$ by a non-alkoxide sol-gel method: From gel to crystalline powders. *J. Eur. Ceram. Soc.* **2015**, *35*, 105.
(50) Sayed, F. N.; Grover, V.; Bhattacharyya, K.; Jain, D.; Arya, A.; Pillai, C. G. S.; Tyagi, A. K. $Sm_{2-x}Dy_xZr_2O_7$ Pyrochlores: Probing Order-Disorder Dynamics and Multifunctionality. *Inorg. Chem.* **2011**, *50*, 2354.
(51) Michel, D.; y Jorba, M. P.; Collongues, R. Study by Raman spectroscopy of order-disorder phenomena occurring in some binary oxides with fluorite-related structures. *J. Raman Spectrosc.* **1976**, *5*, 163.
(52) Kaliyaperumal, C.; Sankarakumar, A.; Palanisamy, J.; Paramasivam, T. Fluorite to pyrochlore phase transformation in nanocrystalline $Nd_2Zr_2O_7$. *Mater. Lett.* **2018**, *228*, 493.
(53) Mandal, B.P.; Garg, N.; Sharma, S. M.; Tyagi, A.K. Preparation, XRD and Raman spectroscopic studies on new compounds $RE_2Hf_2O_7$ (RE = Dy, Ho, Er, Tm, Lu, Y): Pyrochlores or defect-fluorite? *J. Solid State Chem.* **2006**, *179*, 1990.
(54) Chervin, C. N.; Clapsaddle, B. J.; Chiu, H. W.; Gash, A. E.; Satcher, J. H.; Kauzlarich, S. M. Aerogel Synthesis of Yttria-Stabilized Zirconia by a Non-Alkoxide Sol-Gel Route. *Chem. Mater.* **2005**, *17*, 3345.
(55) Feinberg, A.; Perry, C. H. Structural disorder and phase transitions in ZrO_2-Y_2O_3 system. *J. Phys. Chem. Solids* **1981**, *42*, 513.
(56) Vasanthavel, S.; Derby, B.; Kannan, S. Tetragonal to Cubic Transformation of SiO_2-Stabilized ZrO_2 Polymorph through Dysprosium Substitutions. *Inorg. Chem.* **2017**, *56*, 1273.
(57) Lázár, I.; Kalmár, J.; Peter, A.; Szilágyi, A.; Győri, E.; Ditrói, T.; Fábián, I. Photocatalytic performance of highly amorphous titania-silica aerogels with mesopores: The adverse effect of the in situ adsorption of some organic substrates during photodegradation. *Appl. Surf. Sci.* **2015**, *356*, 521.
(58) Kolen'ko, Yu.V.; Garshev, A.V.; Churagulov, B.R.; Boujday, S.; Portes, P.; Colbeau-Justin, C. Photocatalytic activity of sol-gel derived titania converted into nanocrystalline powders by supercritical drying. *J. Photoch. Photobio. A* **2005**, *172*, 19.
(59) Li, H.; Li, G.; Zhu, J.; Wan, Y. Preparation of an active SO42-/TiO_2 photocatalyst for phenol degradation under supercritical conditions. *J. Mol. Catal.* **2005**, *226*, 93.
(60) Moussaoui, R.; Elghniji, K.; ben Mosbah, M.; Elaloui, E.; Moussaoui, Y. Sol-gel synthesis of highly TiO_2 aerogel photocatalyst via high temperature supercritical drying. *J. Saudi Chem. Soc.* **2017**, *21*, 751.

DOI: 10.1021/acs.inorgchem.9b01965
Inorg. Chem. 2019, 58, 14467−14477